Inelastic Solution for Power Law Fluid with Taylor Galerkin-Pressure Correction Finite Element Method: Axisymmetric Contraction Flows

A. Sharhan[†] and A. Al-Muslimawi

Department of Mathematics, College of Science, University of Basrah1, Basrah, 61004, Iraq

†*Corresponding Author Email: eala.khashab.sci@uobasrah.edu.iq*

ABSTRACT

In this study we examine the flow of inelastic fluids with various shear properties in axisymmetric contractions with various contraction ratios are selected as 4:1, 6:1 and 8:1 with both rounded-corner and sharp. Particular attention is paid to the effect of shear thickening and shear thinning upon the solution behavior. Power-law inelastic model is employed coupling with the conservation of momentum equation and continuity equation. The numerical simulation of such fluid is performed by using the Taylor Galerkin pressure correction (T-G/P-C) finite element algorithm. The effects of geometry structure and many factors such as Reynolds number (Re) and the parameters of power law model are presented in this study. Particularly, in this study we are focused on the influence of these factors on the solution components and the level of convergence. This research was a comparative study between sharp and rounded-corner contraction geometries with a ratio of 4:1, and to another comparative study among sharp contraction geometries with ratios of 4:1, 6:1, and 8:1. The practical implications of this study focused on vortex length and the impact of varying the parameters of the power law model and the Reynolds number (*Re*) on it for 4:1 contraction flow. The study dealt with the effect of different geometries on the rates of convergence of velocity and pressure as well as the characteristics of axial velocity and pressure on the axis of symmetry.

1. INTRODUCTION

A wide variety of contraction flows, both Newtonian and non-Newtonian which do not fulfll Newton's law of viscosity (see Tanner, 2000)., have been studied in depth, including 4:1 flows, see (Sharhanl & Al-Muslimawi, 2021) and (Ferrás et al., 2014), 6:1 flows, see (Blanco et al., 2019) and (Agelinchaab & Tachie, 2006), and 8:1 flows, see (Haward et al., 2010) and (Lanzaro & Yuan, 2011). Ink-jet printing, fiber-spinning, porous-media flows, blood circulation, and mucin-solution flows in the lungs represent examples of the many fields that use of inelastic fluid flows via contraction geometries. For this type of fluids, the continuity equation for the conservation of mass and the time-dependent equation for the conservation of momentum represent the principle equations (Galdi, 2011) . Additionally, the relationship between the shear rate and the shear stress inside these fluids may be defined as nonlinear. Thus and for this purpose It is necessary to employ the constitutive equations to treat the non-linearity behavior of shear stress. The Binding model, Bird-Carreau, modified power

law, Herschel-Bulkley model, cross model, Carreau model, Carreau-Yasuda model, and Modified Casson model are only a few examples of models for these constitutive equations, (Bharti et al., 2022), (Karimi et al., 2014), (Carer et al., 2021), (Boyd et al., 2007) and (Liepsch et al., 2018) . But one of the most well-known is the power law (shear-thinning, shear-thickening) model (Graham & Jones, (1994), which is represented by: $\mu = k\,(\dot{\gamma})^{n-1}$,

where n is a power-law index, k is a consistency parameter and $\dot{\gamma}_1$ is a shear rate function dependent on second invariant (II_d), (Sharhanl & Al-Muslimawi, 2021) and (Bharti et al., 2022). In order to handle the continuity and momentum equations, a Taylor Galerkin Pressure Correction finite element method (T-G/P-C) is used in this issue under isothermal conditions with no consideration of body forces. A time stepping Taylor Galerkin pressure correction scheme (T-G/P-C) is an essential numerical approach inside the finite element framework (Hawken et al., 1990), for more details see Belblidia et al. (2003). The Taylor–Galerkin technique and the pressure-correction method are the two essential components that

NOMENCLATURE			
u	velocity	$\dot{\gamma}$	shear rate in non-dimensional form
p	pressure	$\dot{\epsilon}$	strain rate
μ	viscosity in non-dimensional form	II_d	second invariant
μ_1	viscosity in dimensional form	III_d	third invariant
μ_2	refrence values of viscosity	θ	Crank-Nicolson parameter
ρ	density	k	consistency parameter in non-dimensional form
n	power law index	k_1	consistency parameter in dimensional form
$\dot{\gamma}_1$	shear rate in dimensional form	k_2	refrence values of share rate
$\dot{\gamma}_2$	refrence values of share rate	Re	Reynolds number
d	deformation rate	d_z	vortex length

make up this strategy. The Taylor–Galerkin method is a two-step Lax-Wendroff time incremental method (expectation corrector), which is essential dependent on a Taylor series expansion in time see (Alzahrani et al., 2020). In order to guarantee second-order precision in time, the pressure-correction approach takes the incompressibility restriction into account. In the present work, sets of differential equations are solved using a time-stepping Taylor Galerkin pressure correction finite element technique (T-G/P-C). The method is used with FE meshes that are triangular in shape, with velocity components at all node vertices and mid-side nodes and pressure nodes at the mid-side nodes. A given domain is treated as a collection of subdomains in the finite element approach, and the governing equation is approximated over each subdomain by any of the classic variation methods or any acceptable method (Reddy, 2019). The inelastic fluid flow through the contraction channels causes turbulence zones within the flow channel. The idea of turbulence may be thought of as a tangled web of vortex filaments, and a significant portion of the physics of turbulence can be adequately described by using the principles of vortex dynamics. A vortex is an area in fluid dynamics where the flow spins around a straight or curved placebo axis. Although the idea of vortices has been around for as long as the study of hydrodynamics, there has never been a consensus on what exactly a vortex is (Jeong, & Hussain, 1995). We focused on the effects of geometry variation, the power law consistency parameter (k), the power law index (n) and (Re) on vortex length for 4:1 contraction flow. The streamwise separation between the cylinder's rear stagnation point and contraction wall, often abbreviated as d_z, is known as the vortex length (Karlson et al., 2020).

The novelty in this study is the comparison and study of the behavior of inelastic fluids for 4:1, 6:1 and 8:1 contraction flows. Also study the behavior of velocity and pressure on the axisymmetric line of the channel flow. Another feature of the novelty of this study was using Taylor-Glerkin / Pressure-Correction finite element method(T-G/P-C) in power law inelastic fluid flow in contraction channel.

The following is a summary of the study. Problem specification and boundary conditions have been described in Section 2. Mathematical modelling is discussed in Section 3. The discussion then moves on to Section 4, where a numerical technique is presented. In Section 4, the algorithm is used to describe and illustrate the numerical technique.. Finally, the results and conclusions are presented clearly in Sections 5 and 6.

2. PROBLEM SPECIFICATION AND BOUNDARY CONDITION

As a starting point for this investigation, we consider the flow of an isothermal inelastic fluid through a two-dimensional axisymmetric channel with 4:1 rounded-corner contraction, 4:1 sharp contraction, 6:1 sharp contraction and 8:1 sharp contraction. In all geometries the widths of the main section are respectively, 4, 4, 6 and 8 units and the width of contraction section for all geometries 1 unit, (for more details, see Fig. 1). The domain of the flow is split into triangular elements, and those elements make up the mesh of geometry (see Fig. 2). The characteristics of the finite element meshes used in our research are outlined in Table 1 which obtained by split the domain to these number of elements and generated the mesh.

Boundary conditions (*BCs*)**:** The configuration of the BCs ie presented as follows:

(a) Poiseuille (Ps) flow $(u_z = u_{max}(1 - \frac{r^2}{R^2})$, R=inlet diameter) is applied at the inlet and vanishing radial velocity.

(b) No-slip boundary conditions at the wall are enforced.

(c) There is no pressure and free axial velocity being exerted at the outflow of the channel, also no radial velocity in the axisymmetric line.

We intended that the length of the main section of the channel (L_w) be longer than the contraction section of the channel (L_c). So that the length of the main section is greater than twice the length of the contraction section.

Figure 1 provides an explanation for each of the aforementioned aspects of boundary conditions, such that $C_r = \frac{D}{D_c} = 4/1$, where C_r denoted contraction ratio and other dietials of boundaries find it in Table 2

3. MATHEMATICAL MODELING

The governing equations for incompressible inelastic flow under isothermal conditions when body forces are disregarded consist of the continuity and momentum
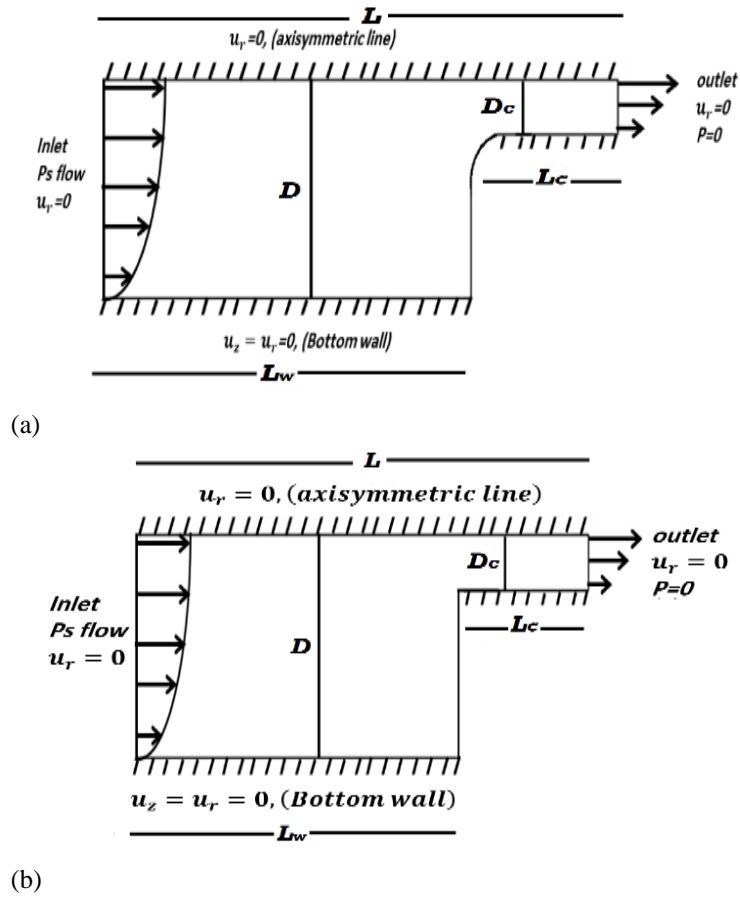
equations. These equations are defined as follows:

(a)

(b)

Fig. 1 Flow geometry (a) 4:1 rounded-corner contraction (b) 4:1 sharp contraction
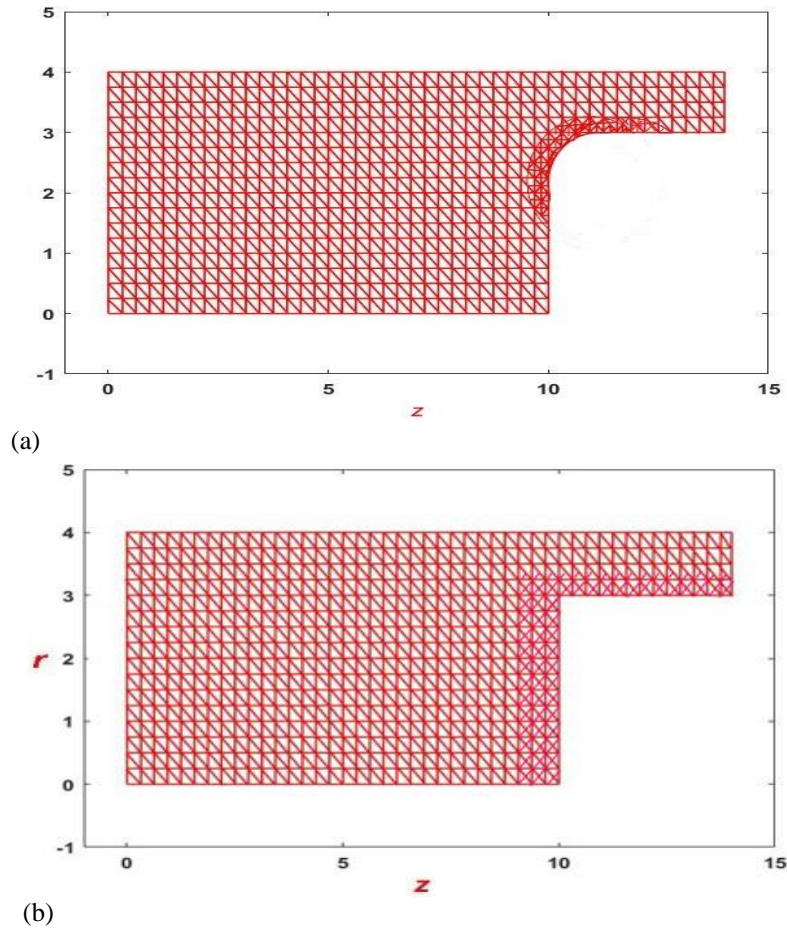

(a)

(b)

Fig. 2 Structured finite element meshes (a) 4:1 rounded-corner contraction (b) 4:1 sharp contraction

Table 1 Statistically of meshes elements

Mesh	Total Elements	Total Nodes	Boundary Nodes	Pressure Nodes
4:1rounded-contraction	1192	2438	268	642
4:1 sharp contraction	1128	2387	244	639
6:1 sharp contraction	1640	3419	276	890
8:1 sharp contraction	2152	4460	308	1154

Table 2 Statistically of boundaries and diametrs length

L	L_w	D	L_c	D_c
14	10	4, 6, 8	4	1

$$\nabla \cdot u = 0, \tag{1}$$

$$\rho \left(\frac{\partial u}{\partial t} + u \cdot \nabla u \right) = -\nabla p + \nabla \cdot (2\mu(\dot{\gamma}, \dot{\varepsilon})d), \tag{2}$$

see (Aboubacar et al., 2002), where u, ρ, p, and μ are represent the velocity, density, hydrodynamic pressure, and viscosity respectively. Also the rate of deformation is denoted by $d = \frac{1}{2}(\nabla u + \nabla u^\tau)$, while the derivative operator is denoted by ∇. Additionally, the symbols $\dot{\varepsilon}_1$ and $\dot{\gamma}_1$ stand for the strain and shear rates of extensional flow and shear flow, respectively, such that:

$$\begin{aligned} \dot{\gamma}_1 &= 2\sqrt{II_d} \\ \dot{\varepsilon}_1 &= 3\frac{III_d}{II_d} \end{aligned}. \tag{3}$$

In an axisymmetric coordinate system, the second and third invariants of the shear rate and rate of strain tensor can be defined as follows (Yasir et al., 2020):

$$II_d = \frac{1}{2}\text{tr}\,(d^2) = \frac{1}{2}\left\{ \left(\frac{\partial u_r}{\partial r}\right)^2 + \left(\frac{\partial u_z}{\partial z}\right)^2 + \left(\frac{u_r}{r}\right)^2 + \frac{1}{2}\left(\frac{\partial u_r}{\partial z} + \frac{\partial u_z}{\partial r}\right)^2 \right\}, \tag{4}$$

$$III_d = \det(d) = \frac{u_r}{r}\left\{ \frac{\partial u_r}{\partial r}\frac{\partial u_z}{\partial z} - \frac{1}{4}\left(\frac{\partial u_r}{\partial z} + \frac{\partial u_z}{\partial r}\right)^2 \right\}. \tag{5}$$

Furthermore, the scaling may be used to establish the Reynolds number $Re = \rho\frac{UL}{\mu}$ with non-dimensions, where U, L, and ρ are the velocities, lengths, and densities, respectively. In this particular case, the equation for the non-dimensional momentum of a general Newtonian fluid may be stated as follows (see (Aboubacar et al., 2002)):

$$\frac{\partial u}{\partial t} = \frac{1}{Re}[\nabla \cdot (2\mu d) - Re\ u \cdot \nabla u - \nabla p]. \tag{6}$$

In this research, the power-law model is applying to illustrate this study where power-law model in dimensional form is;

$$\mu_1 = k_1(\dot{\gamma}_1)^{n-1}. \tag{7}$$

For μ_2, k_2, and $\dot{\gamma}_2$ are denoted the refrence values of viscosity, consistency parameter and shear rate, respectively, then the power law model in non-dimesional form as (see Thohura, S. et al, 2019):

$$\frac{\mu_1}{\mu_2} = \frac{k_1}{k_2}\left(\frac{\dot{\gamma}_1}{\dot{\gamma}_2}\right)^{n-1}, \tag{8}$$

for $\frac{\mu_1}{\mu_2} = \mu$, $\frac{k_1}{k_2} = k$ and $\frac{\dot{\gamma}_1}{\dot{\gamma}_2} = \dot{\gamma}$ then the final non-dimensional form of power low model is

$$\mu = k(\dot{\gamma})^{n-1}. \tag{9}$$

In the first part of this work, we established definitive values for all of the model's parameters (Introduction).

4. NUMERICAL METHOD

Utilizing a fractional step methodology, three steps make up (T-G/P-C) finite element method (D.M. Hawken et al., 1990). Starting with the initial velocity and pressure fields as inputs, we employ a two-step predictor-corrector approach to determine the u^* ingredients. The Choleski technique is used to calculate the pressure differences $(p^{n+1} - p^n)$ in the second stage, with u^* acting as the governing variable. The third stage involves making an estimation for the velocity field u^{n+1} using the mid-velocity u^* and pressure differences $(p^{n+1} - p^n)$. The weak formulation was used as a starting point for the application of the finite element approach, which finally resulted in the derivation of algebraic equations represented by matrices. Where it has been abbreviated by equations from (10) to (13).

Then this leads directly to the fractional step being written as follows:

$$\text{Stage1a:}\frac{2Re}{\Delta t}\left[u^{n+\frac{1}{2}} - u^n\right] = L(u^n, d^n) - \nabla p^n, \tag{10}$$

$$\text{Stage1b:}\frac{Re}{\Delta t}[u^* - u^n] = L\left(u^{n+\frac{1}{2}}, d^{n+\frac{1}{2}}\right) - \nabla p^n, \tag{11}$$

$$\text{Stage2:}\nabla^2(p^{n+1} - p^n) = \frac{Re}{\theta\Delta t}\nabla \cdot u^*, \tag{12}$$

$$\text{Stage3:}u^{n+1} = u^* - \frac{\theta\Delta t}{Re}[\nabla(p^{n+1} - p^n)]. \tag{13}$$

Where,

$$L(u, d) = [\nabla \cdot (2\mu(\dot{\gamma}, \dot{\varepsilon})d) - Re\ u \cdot \nabla u]. \tag{14}$$

The Crank-Nicolson approach, which has superior precision and stability over other methods and reduces time errors in the time-stepping scheme, is the methodology used in the solution for $\theta = 1/2$, (J. Crank & P. Nicolson 1996). Then, the matrix form of the corresponding (T-G/P-C) finite element method from Equations (8), (9), (10), and (11) may be expressed as: see (Hawken et al., 1990).

$$\text{Step1a:}\left[\frac{2Re}{\Delta t}M + \frac{1}{2}S\right]\left(U^{n+\frac{1}{2}} - U^n\right) = \{-[S + Re\ N(U)]U + \ell^T P\}^n, \tag{15}$$

$$\text{Step 1b: }\left[\frac{Re}{\Delta t}M + \frac{1}{2}S\right](U^* - U^n) = \{-SU + \ell^T P\}^n - Re\ [N(U)U]^{n+\frac{1}{2}}, \tag{16}$$

Step2: $K(P^{n+1} - P^n) = -\frac{Re}{\theta \Delta t}\ell U^*$, (17)

Step3: $\frac{Re}{\Delta t}M(U^{n+1} - U^*) = \theta \ell^T(P^{n+1} - P^n)$, (18)

where U^* is the intermediate nodal velocity vector established in Step 1b, and the other four vectors U^n, U^{n+1} and P^n, P^{n+1} reflect the velocities and pressures at the nodes at times t^n and t^{n+1}, respectively. The matrices for mass, momentum diffusion, convection, divergence/pressure gradient, and pressure stiffness are denoted by the letters *M, S, N, ℓ,* and *K,* respectively (López-Aguilar et al., 2015). According to the matrix notation

$$M_{ij} = \int_{\Omega}\phi_i\phi_j d\Omega, \ K_{ij} = \int_{\Omega}\nabla\psi_i\nabla\psi_j d\Omega,$$

$$N(U)_{ij} = \int_{\Omega}\phi_i(U^n.\nabla\phi_j)d\Omega, \ (\ell)_{ij} = \int_{\Omega}\psi_i(\nabla.\phi_j)\,d\Omega,$$

$$(S)_{ij} = \int_{\Omega}\mu(\dot{\gamma}, \dot{\epsilon})[\nabla\phi_i\nabla\phi_j + (\nabla\phi_j)^{\tau}]\,d\Omega$$

5. Results

The following results were obtained via programming the simulations code. Taylor Galerkin pressure correction finite element method is used in this study to address the problem of constrained inelastic fluid flow through the 4:1 sharp contraction, 4:1rounded-corner contraction, 6:1 sharp contraction, and 8:1sharp contraction. This research focuses on the convergence rate and the behavior of the solution components. In addition, the implications of altering the geometric form of the flow channel on the aforementioned research has been discussed. Also this study reached the vortex length in 4:1 contraction flow. Where the research was make up to a comparison of two sections. The first consisted of a 4:1 rounded-corner contraction and a 4:1 sharp contraction, while the second consisted of a 4:1 sharp contraction, a 6:1 sharp contraction, and an 8:1 sharp contraction.

Figures 3 and 4 show, respectively, the velocity and pressure fields of an inelastic fluid flow axisymmetric 4:1 rounded-corner and sharp contraction geometries. Both of these contractions have a ratio of 4:1. With the parameters $\{Re = 1, k= 1,$ and $n = 0.8\}$, it is possible to see a pressure difference and a small difference in velocity. It is observed that in the case of a rounded-corner contraction, the maximum velocity is lower than in the case of a sharp contraction. It is common knowledge that $A_1 u_1 = A_2 u_2$, which may be expressed mathematically as the continuity equation (Şahin et al., 1995). In this equation, A_1 and u_1 stand for the area and velocity in the broad part of the flow channel, while A_2 and u_2 stand for the area and velocity in the narrow part of the flow channel. This indicates that there will be a reduction in velocity if the area in the narrow portion of the channel is increasing. Since the diameters of the two channels are the same but the angle of contraction differs, curving the angle of contraction necessitates a bigger area for the narrow section of the channel than if the angle of contraction is sharp, which results in a reduction in velocity. As a result, we see that the velocity in the flow channel with a rounded-corner contraction is smaller than the velocity in the flow channel with a sharp contraction.

(a)

(b)
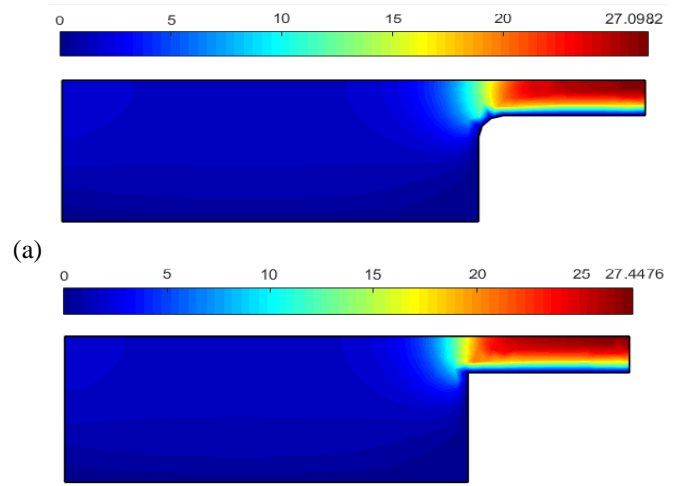
Fig. 3 Velocity field with $\{Re = 1, k= 1,$ and $n = 0.8\}$ (a) 4:1 rounded-corner contraction (b) 4:1 sharp contraction

(a)

(b)
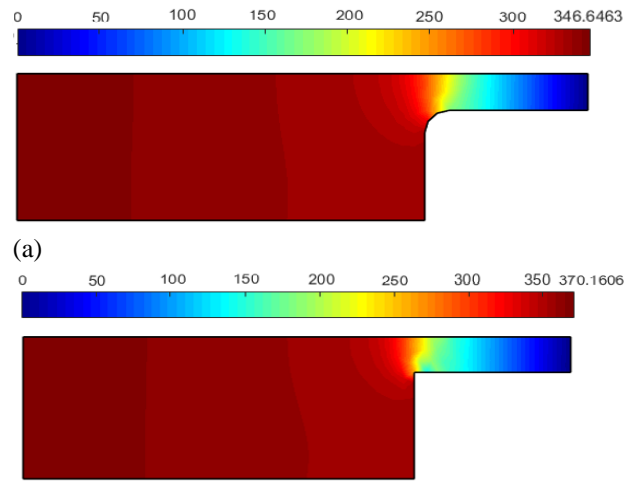
Fig. 4 Pressure field with $\{Re = 1, k= 1,$ and $n = 0.8\}$, (a) 4:1 rounded-corner contraction (b) 4:1 sharp contraction

The rate of convergence of axial velocity and pressure are depicted in Fig. 5 and Fig. 6, respectively for both flows 4:1 rounded-corner contraction and 4:1 sharp contraction in the case of (a) shear thinning with $n = 0.8$ and (b) shear thickening with $n = 1.6$ at fixed $\{Re = 8$ and $k =1\}$. The findings indicate that the convergence rate of velocity and pressure for both shear thinning and shear thickening in the sharp contraction is less than that for the rounded contraction.

For$||E(u_z)|| =||u^{n+1} - u^n||_p$and $||E(p)|| = ||p^{n+1} - p^n||_p$ must both be $\leq TOL$, where (TOL=10^{-6}), denoted the tolerance value of error. Also $\Delta t = 10^{-3}$

Using the fixed parameters $\{Re = 1, k = 1\}$, Fig. 7 depicts the relationship between the power-law index (n) and maximum level of velocity along the axis of symmetry. According to the findings, increasing the values of n leads to a discernible rise in the maximum velocity of the fluid flow in both flows sharp and rounded contraction for the level of n from 0.2 to 3, which reflects a direct correlation between the value of n and
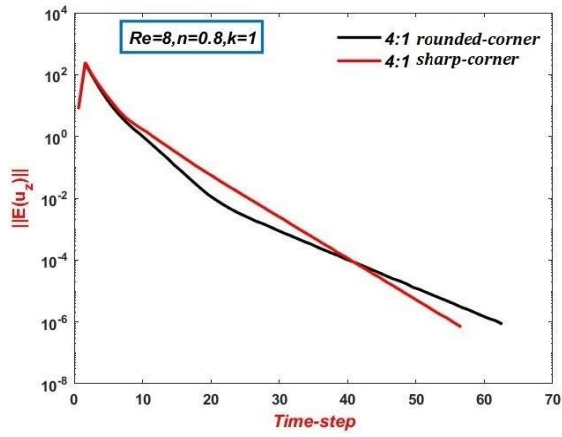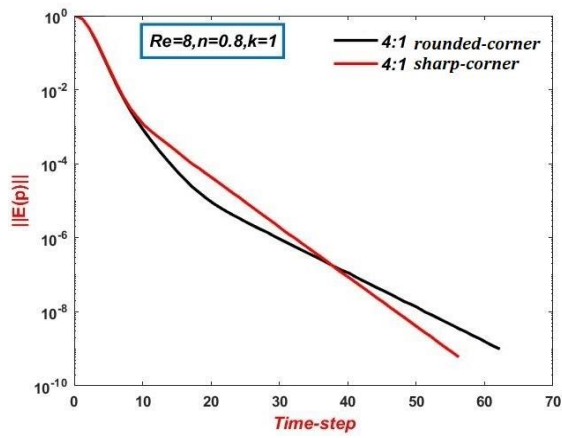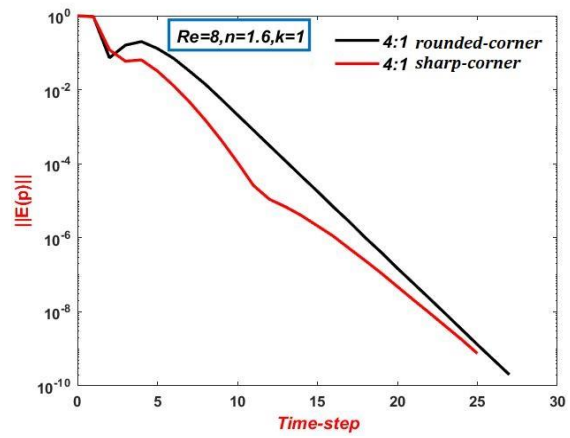
(a)
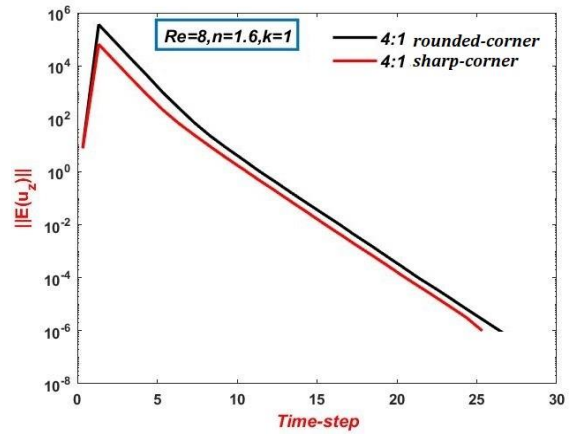
(b)

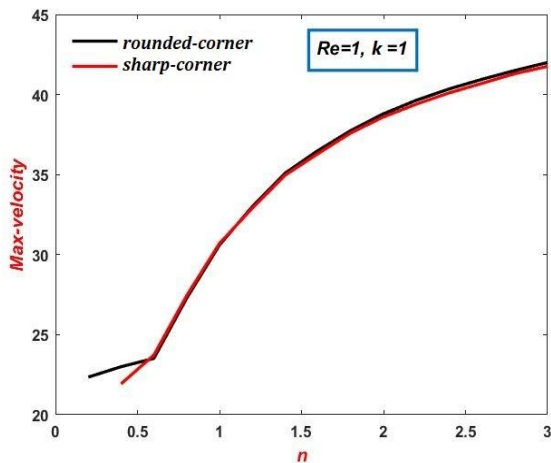**Fig. 5 Convergence of velocity; *Re*=8, *k*=1 (a) shear thinning, (b) shear thickening**

(a)

(b)

**Fig. 6 Convergence of pressure; *Re*=8, *k*=1 (a) shear thinning, (b) shear thickening**

**Fig. 7 Maximum velocity along centreline; n-variation, *Re* =1, *k* =1**

the maximum velocity. Due to the effect of pressure increasing on the fluid and rise in viscosity, particularly towards the inner walls of the channel, then the velocity falls near the walls and increases along the centerline to alleviate the increased pressure. This is supported by the evidence presented in (Mahmood et al., 2022). Since the two Figs are subject to the same criteria in the flow that occurs between them, there is very small a discernible

difference in the curves that represent the relationship between *n* and the maximum velocity and Fig. 3 reinforces that finding.

Figure 8 depicts the relationship that exists between the parameter *n* and the time step, under {*Re* = 1 and *k* = 1}. The findings demonstrated that the time step is as little as feasible when *n* approaches to 1 from the right or left. Here, insignificant difference is observed between. This indicate that the rate of convergence in Newtonian fluid is less than of convergence rate of non-Newtonian fluid.
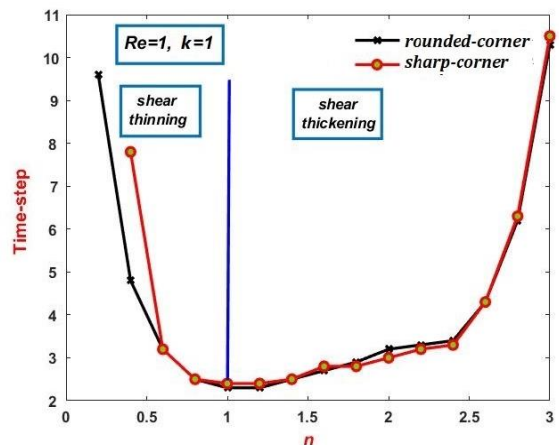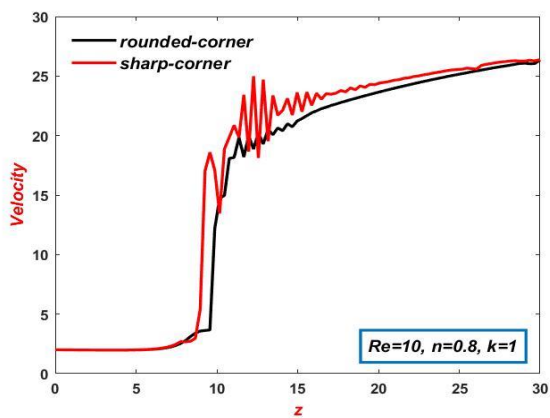

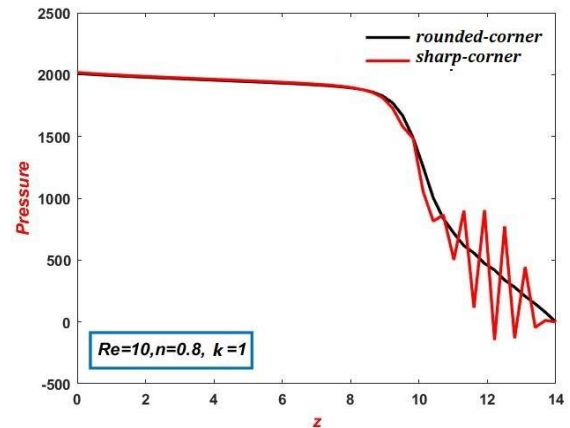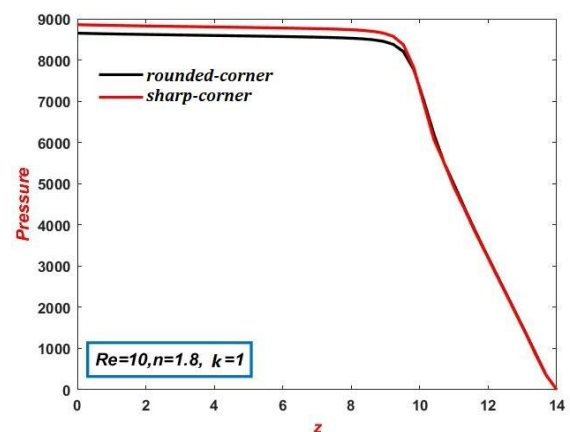**Fig. 8 Power law index (*n*) vs. time step, *Re*=1, *k*=1**
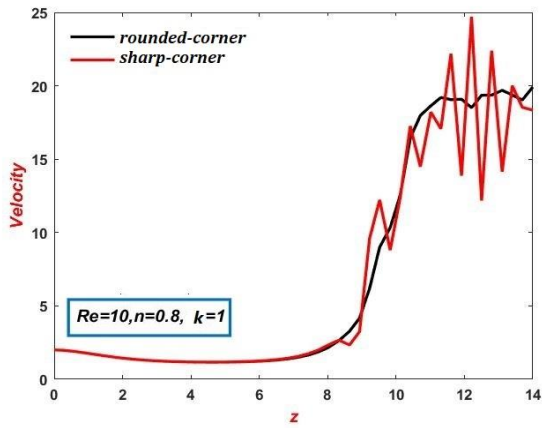
(a)
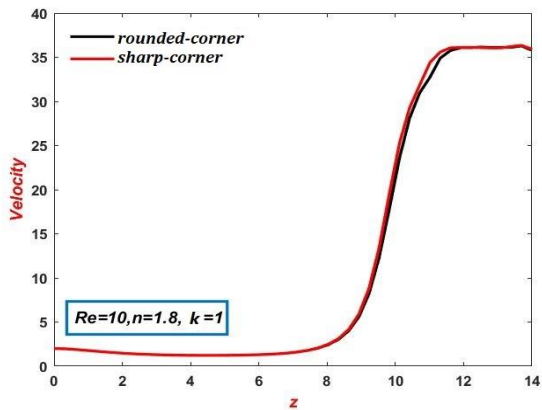
(b)

(c)

Fig. 9 Velocity on the symmetrical axis; Re=1 , *k*=1, (a) Shear thinning, (b) shear thickening, (c) contraction section =20

(a)

(b)

Fig. 10 Pressure on the symmetrical axis; *Re* =1 , *k*=1, (a) Shear thinning, (b) shear thickening

Both flows rounded and sharp due to the closeness of their real size and their subjection to the same flow conditions. The profiles depict the relationship between *n* and the time step for both flows can be seen to vary somewhat in the case of shear thinning. In contrast, for the shear thickening there is hardly any discernible difference in both cases.

Figures 9 and 10 show the behavior, of axial velocity and pressure along the symmetry axis with the fixed parameters {$Re = 10$ and $k = 1$}. Here, the profiles are plotted for both fluids shear thinning with $n=0.8$ and shear thickening with $n=1.6$. The results reveal that, the maximum level of velocity is occurred near of the contraction region, due to the channel's extreme narrowness, which is consistent with the physical facts and the results of others (Walker et al., 2011). In addition, from the comparison between sharp and rounded cases one cannot see any significant change in the level of velocity along the channel. Also one can observe that in the case of shear thinning the flow through rounded-corner contraction is more stable than that with sharp-corner contraction. In fact, the sudden sharp contraction of the flow channel causes a disturbance in the fluid flow, making its velocity fluctuate up and down. Also, the large difference in velocity before and after the fluid enters the narrow part of the flow channel has a significant impact on the fluctuation of the velocity level within the narrow part of the channel. Therefore, we notice that the velocity level in the narrow part of the channel is instable in the case of shear thinning compared to shear thickening case. In contrast, we see an opposite feature in the case of pressure drop, where the profiles in Fig. 10 provide that the maximum level of pressure in both channels at the inlet (Schäfle & Kautz, 2019). For inlet flow we applied the Poiseuille flow with max-velocity is 2, see (Fadhel & Al-Muslimawi, 2020).

The fluctuation in the rate of velocity on the axis of symmetry in Fig. 9 (a) becomes stable as the length of the contraction section increases in the channel. This can be clearly seen in Fig. 9 (c), where stability appears in the rate
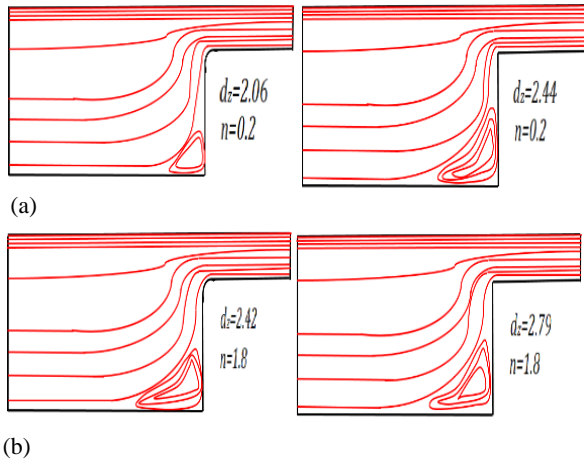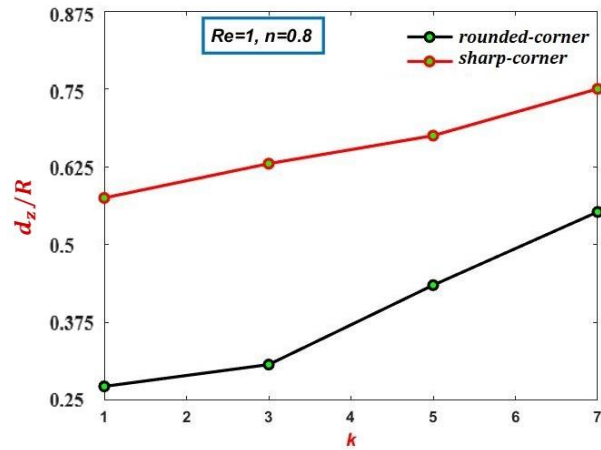
Fig. 11 Scheme of streamline for 4:1 rounded-corner and sharp contraction with {*Re*=1, *k*=2} *n* variation, (a) *n*=0.2, (b) *n*=1.8
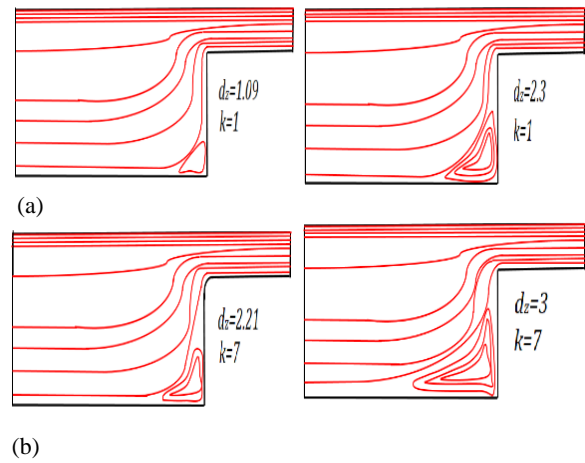
Fig. 13 Scheme of streamline for 4:1 rounded-corner and sharp contraction with {*n*=0.8, *Re*=1} and *k* variation, (a) *k*=1, (b) *k*=7
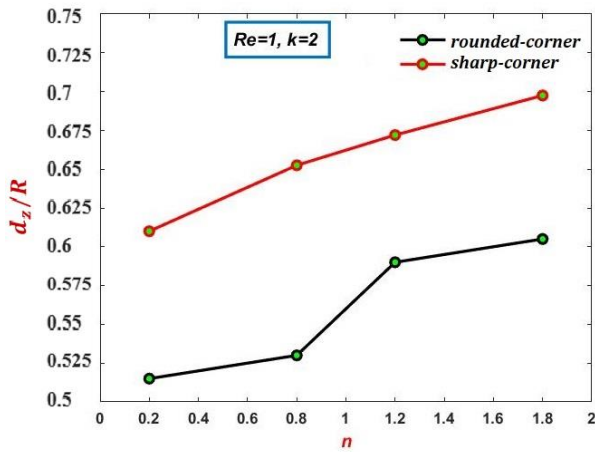
Fig. 12 Vortex length vs function of n; *Re*=1, *k*=2

Fig. 14.Vortex length vs faunction; of *k*; *Re* =1, *n* =0.8

of velocity as we move away from the first point of contraction.

In the field of fluid dynamics, a vortex is an area in a fluid in which the flow spins around an axis of rotation, that can be either straight or curved. Vortex length (d_z) is an expression that refers to the distance between the separation point in this region and the contraction plane indicated in Fig. 11, (Sousa et al., 2011). The length of a vortex (d_z) is affected by different of factors, including pressure, velocity, the type of flow, laminar or turbulent, Reynolds number (*Re*), viscosity, and geometric cross-sectional area of the flow channel (Alves et al., 2005) and (Thorne & Blandford, 2017). Thus, we have been keen to study the effect of some factors on the Vortex length (d_z).

. ***n-variation:*** The impact of varying the value of power-law index *n* on the vortex length for {*Re* =1, *k* = 2} is shown in Fig. 11 for a variety of contraction geometries of streamline (4:1 sharp contraction and rounded contraction). Substantial vortex enhancement is observed through upstream vortex intensity and cell-size increase as *n* increases.

Figure 12 shows that the vortex length is a function of *n* corresponding to both flows sharp-corner and rounded-corner at {*Re*=1, *k*=2}. Results on vortex length reveal, as

reported by others (Ameur, 2018), that in both geometries vortex length is rised as the values of *n* increases. In this context, one can see that the vortex length in the case of sharp-corner contraction is longer than that in the case of rounded-corner contraction

k-variation: The results of the vortex length with the variation in *k* values for various geometries and the value of the constant parameter {*Re* = 1, *n*=0.8} are represented in the Fig. 13. The streamline for the flow via the 4:1 contraction channels is shown geometrically in Fig 13, whether it is rounded-corner or sharp. Where the vortex's overall behavior corresponds to the vortex's behavior in Fig. 11.

As can be seen in Fig. 14, there is a positive relationship between *k* and the vortex length: as the length of the vortex increases, so does the value of *k*. It's also worth noting that the geometry's surface area has an impact; doing so while keeping the same outlet results in a longer vortex. For a rounded-corner contraction, the vortex length is less than that for a sharp contraction.

Re-variation: Fig. 15 that follow demonstrate the impact of varying the values of *Re* on the length of the
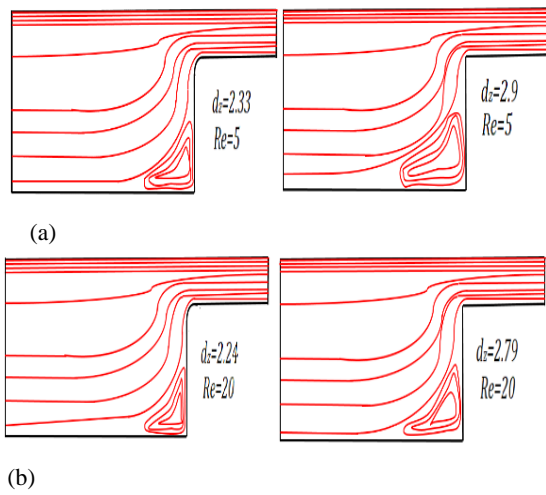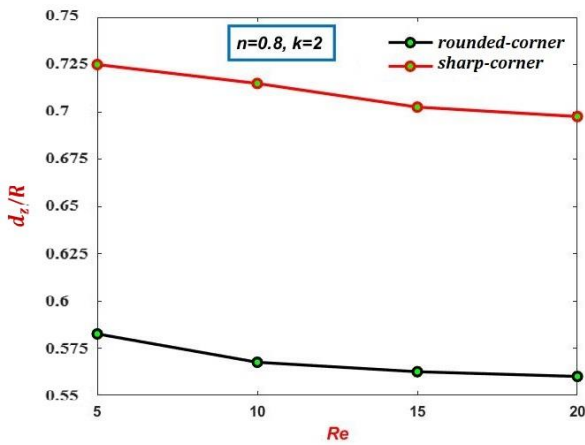
Fig. 15 Scheme of streamline for 4:1 rounded-corner and sharp contraction with {n=0.8, k =2} and *Re* variation, (a) *Re* =5, (b) *Re* =20
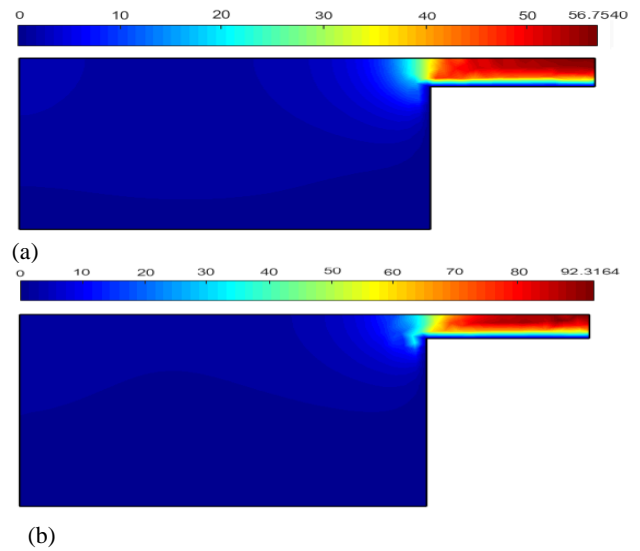

Fig. 16 Vortex length vs function of *Re*; n=0.8, k =2

vortex with fixed parameters {n=0.8, k=2}. Figure 16 illustrates an inverse relationship between *Re* and vortex length, where the vortex length (d_z) decreases as *Re* rises. Furthermore, the results showed that the vortex length is significantly and clearly influenced by the geometry difference. Greater values for the length of vortices are produced by the sharp-corner contraction geometry compared to rounded-corner geometry.

Again, the vortex length is presented as a function of *Re* under same setting of parameters in Fig. 16. The profiles demonstrate that *Re* and vortex length have an inverse relationship, where vortex length decreases as *Re* increases and that is consistent with the findings obtained by the researchers (Karlson et al., 2020). According, the vortex is longer in the case of sharp contraction than a rounded contraction.

For *R* is denoted the inlet diameter of channel we take the normalized of vortex length (d_z/R) vs functions of *n, k* and *Re* are considerd inf Figs 12, 14 and 16.The velocities and pressures are significantly impacted by variations in the size of the flow channels, which have the same outlet. With increasing channel size comes a corresponding rise in the number of elements needed to

Fig. 17 Velocity field with {*Re* = 1, *k*= 1, and *n* = 0.8}; (a) 6:1 sharp contraction; (b) 8:1 sharp contraction

represent the mesh of the channel geometry, where table 1 provides statistical information on these values. The velocity and pressure fields for the 6:1 and 8:1 abrupt contraction flow channels are shown in Figs 17 and 18, respectively, where (a) stands for 6:1 and (b) stands for 8:1 with fixed parameters {*Re* = 1, *k* = 1, *n* = 0.8}. It was previously covered how the 4:1 channel's velocity and pressure fields are described. It seems from these Figs, which depict the pressure and velocity fields, that the quantity of flow velocity at the outflow is vastly different under the impact of the change ratio of area with same diameter of channel outlet. The fluid's velocity at the outlet increases as the inlet part expands.
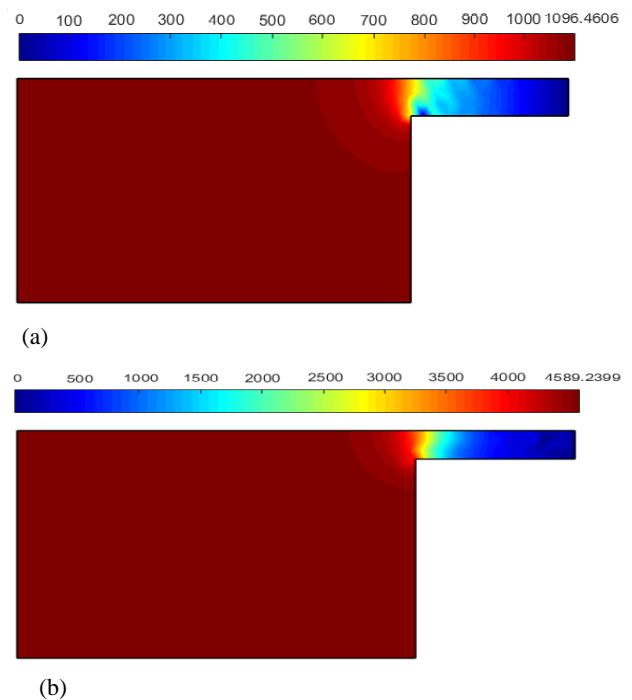
Fig. 18 Pressure field with {*Re* = 1, *k* = 1, and *n* = 0.8}; (a) 6:1 sharp contraction; (b) 8:1 sharp contraction
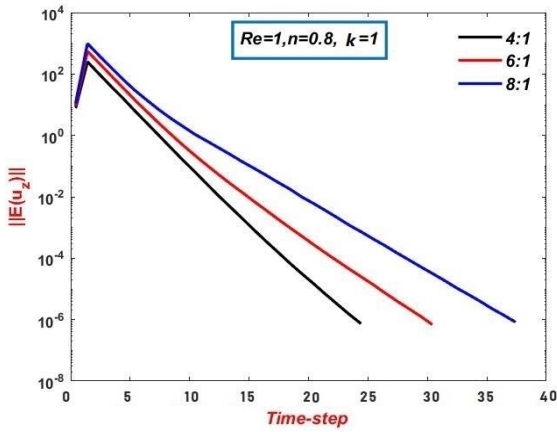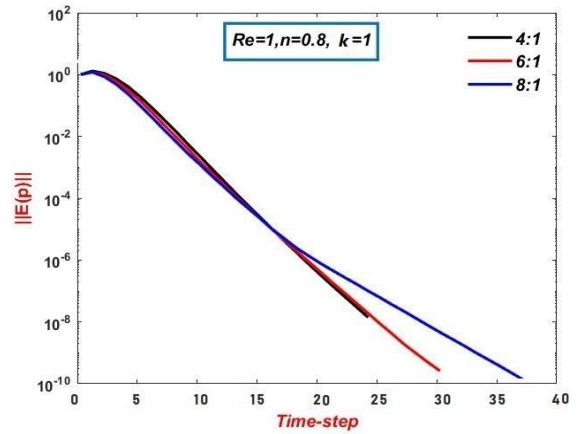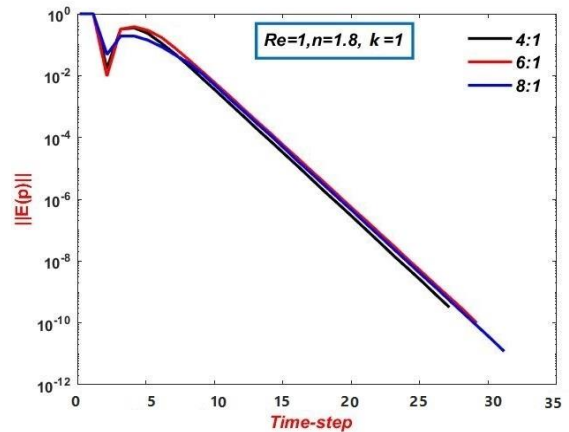
(a)
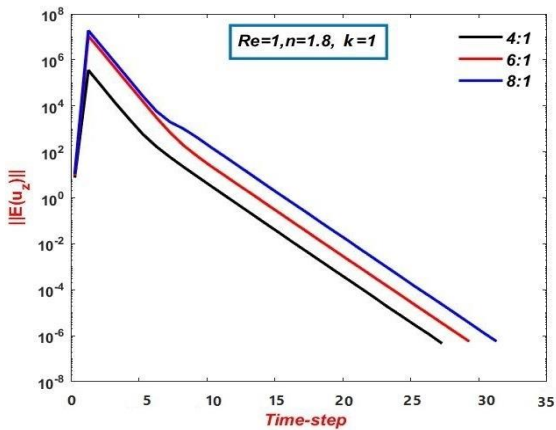
(b

Fig. 19 Convergence of velocity; *Re*=1, *k*=1 ;(a) shear thinning, (b) shear thickening

(a)

(b)

Fig. 20 Convergence of pressure; *Re*=1, *k*=1 ;(a) shear thinning, (b) shear thickening

The general formula for the continuity equation (Şahin et al., 1995) is $(A_1 u_1 = A_2 u_2)$, which provides an explanation for this increase. where $A_1 u_1$ represents the large area of the channel with velocity in it and $A_2 u_2$ represents the narrow area of the channel with velocity in it (the systolic section). While the second section's areas are equal for all channel, the first section's areas of the channels are different. In order to satisfy the continuity equation, the velocity at the exit, denoted by u_2, must dramatically rise as the area of the first section increases.

Convergence of axial velocities and pressures are shown in Figs 19 and 20, with (a) representing shear thinning and (b) representing shear thickening with constant parameters {$Re = 1$, $k = 1$}, respectively with ($n = 0.8$) in shear thinning and ($n = 1.8$), in shear thickening. In both the shear-thinning and shear-thickening scenarios, we find that the convergence rate increases as the mesh area becomes bigger. This is easily seen when using a uniform element size across geometries types; when the geometry area (mesh) expands, more elements are required, therefore the solution time step increases accordingly (Patil & Jeyakarthikeyan, 2018). As a result, we can observe that the convergence rate for channel 8:1 is higher than for channel 6:1, which is higher than for channel 4:1.
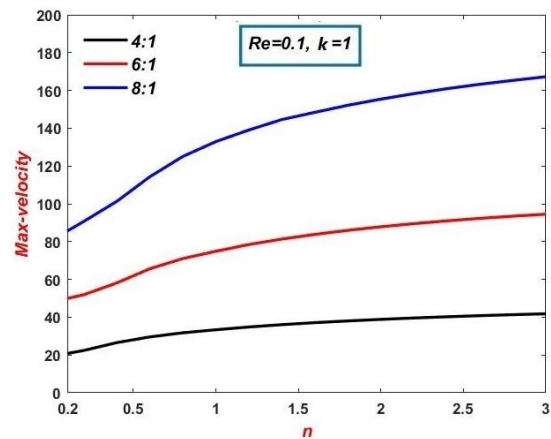
Fixed parameters {$Re = 0.1$, $k = 1$} are used to illustrate the relationship between *n* and the maximum axial velocity in Fig .21. Where it was shown that as *n* values are increased, maximum velocity values are also increased (Sharhanl & Al-Muslimawi, 2021). Figure 17 provides a clear explanation for the observation that the maximum velocity values increased together with the size of the geometric Fige.

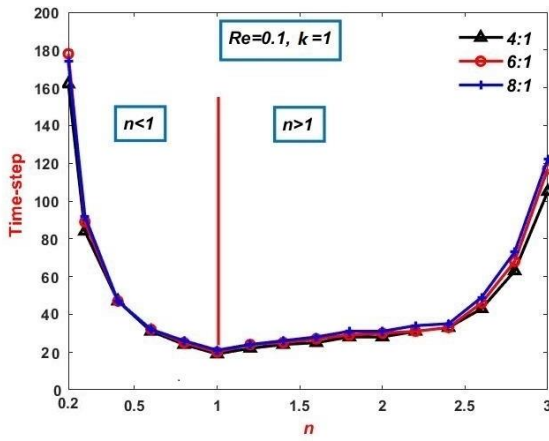**Fig. 21 Maximum velocity along centerline; n-variation, Re=0.01, k=1**

Fig. 22 Power law index (*n*) vs. time step, *Re*=1, *k*=1

Parameters {*Re* = 0.1, *k* = 1} are held fixed in Fig. 22 to illustrate the relationship between *n* and time step. The findings demonstrated that time step rises as shear thickness or thinning increases, as also be shown in (Sharhanl & Al-Muslimawi, 2021). Figure 22 also reveals that the time step rises in channel 8:1 more than in channel 6:1, which is more than in channel 4:1.
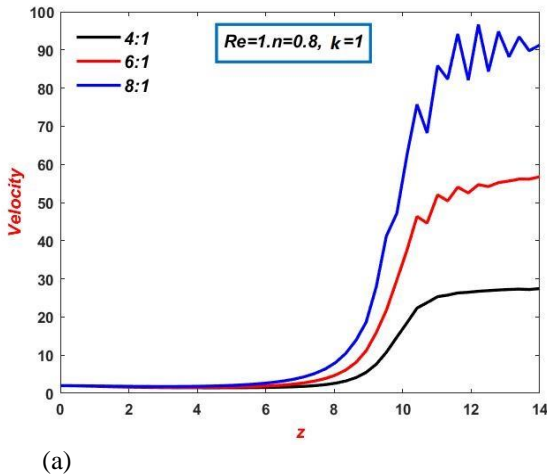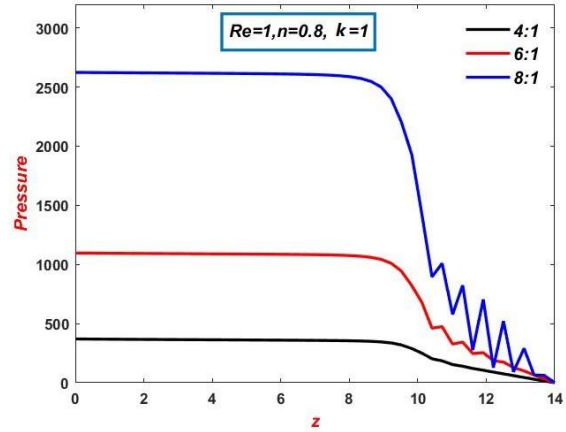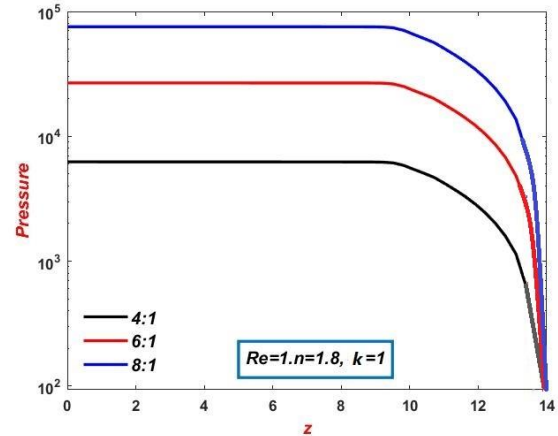

(a)
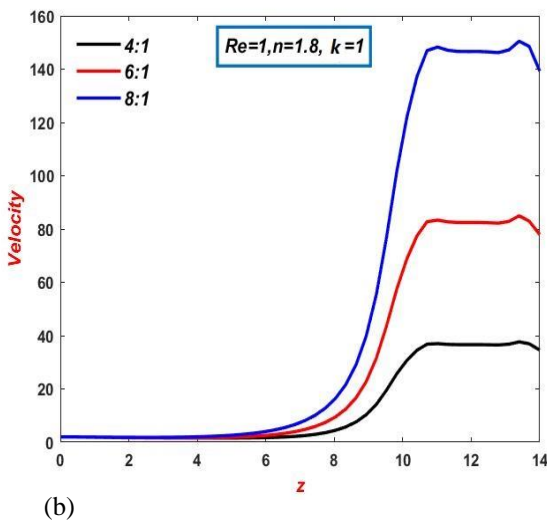
(b)

Fig. 23 Velocity through symmetry axis; *Re*=1, *k*=1, (a) Shear thinning, (b) shear thickening

(a)

(b)

Fig. 24 Pressure through symmetry axis; *Re*=1, *k*=1, (a) Shear thinning, (b) shear thickening

Figures 23 and 24 show the behavior of axial velocity and pressure, respectively, on the axis of symmetry for different geometries of 4:1, 6:1, and 8:1 sharp contraction, with the fixed parameters {*Re* = 1, *k* = 1} and *n* = 0.8 in the case of shear thinning in (a) and *n* = 1.8 in the case of shear thickness in (b). The three curves that depict the axial velocities on the symmetric lines of various geometers demonstrate that the velocities rise as the geometry area grows, as we previously discussed in Figs 17 and 21. Figure 23 shows that when *z* approaches 10, the velocity rapidly rises for all three curves representing the three geometries due to the narrowing of the flow channel and the increase in velocity in the narrow channel. In the case of shear thinning, it seems that the velocity line representing the 8:1 geometry oscillates. This is due to the fact that the difference of velocity before and after narrow section of channel is very big. Accordingly, in shear thickening the line of velocity is stable because the difference of fluid velocity before and after narrow part of channel less than in shear thinning. As for Fig. 24, which represents the behavior of pressure on the axis of symmetry, we notice the behavior of pressure is completely different and opposite to the behavior of velocity in terms of value and direction, and Bernoulli's principle explains this clearly.

6. CONCLUSION

Starting with the Navier-Stokes equations, this study reviews the numerical analysis of the flow of an inelastic fluid via different contraction channels. We investigated the flow in axisymmetric 2D planar contraction channel under isothermal circumstances using a time-stepping Taylor Galerkin Pressure Correction (T-G/P-C) finite element method. According to the findings, sharp contractions had a greater velocities in the 4:1 flow channel compared to rounded-corner contractions. While the rate of convergence of the velocity and pressure of the fluid flow through the rounded-corner contraction channel is greater than the rate of convergence of the velocity and pressure in the flow channel of the sharp contraction. The results also showed that the vortex length is directly related to the parameters of the power law model and has an inverse relationship to the Reynolds number. This was a comparison of the 4:1 flow channels of sharp and rounded-corner contractions. The second part of the results was a comparison among the sharp flow channels only, which are 4:1, 6:1 and 8:1. The results showed that increasing the geometric area of the flow channel leads to an increase in the axial velocity in symmetry line and also increases the rate of convergence of velocity and pressure. The velocity and the rate of convergence of velocity and pressure in the 8:1 flow channel are greater than in the 6:1 flow channel, which in turn is greater than in the 4:1 flow channel.

CONFLICT OF INTEREST

Authors have no conflict of interest to declare.

AUTHORS CONTRIBUTION

Alaa Abdulwahid Sharhan: Writing the abstract for the manuscript, Extracting the results and arranging them according to a scientific format, Interpreting the results that appeared in the research, Writing conclusions for the research; **Alaa. H. Al-Muslimawi**: Writing the introduction, Writing the mathematical model for this work from the equations and equations of the inelastic fluid model, Programming and writing MATLAB code to simulate this problem, A general review of the research before sending to the journal.

REFERENCES

Aboubacar, M., Matallah, H., Tamaddon-Jahromi, H. R., & Webster, M. F. (2002). Numerical prediction of extensional flows in contraction geometries: hybrid finite volume/element method. *Journal of Non-Newtonian Fluid Mechanics,* 104(2-3), 125-164. https://doi.org/10.1016/S0377-0257(02)00015-0

Agelinchaab, M., & Tachie, M. F. (2006). Open channel turbulent flow over hemispherical ribs. International *Journal of Heat and Fluid Flow*, 27(6), 1010-1027. https://doi.org/10.1016/j.ijheatfluidflow.2006.03.001

Alves, M. A., Pinho, F., & Oliveira, P. J. (2005). Visualizations of boger fluid flows in a 4: 1 square–square contraction. *AIChE Journal*, 51(11), 2908-2922. https://doi.org/10.1002/aic.10555

Alzahrani, F., Hobiny, A., Abbas, I., & Marin, M. (2020). An eigenvalues approach for a two-dimensional porous medium based upon weak, normal and strong thermal conductivities. *Symmetry*, 12(5), 848. https://doi.org/10.3390/sym12050848

Ameur, H. (2018). Pressure drop and vortex size of power law fluids flow in branching channels with sudden expansion. *Journal of Applied Fluid Mechanics*, 11(6), 1739-1749. https://doi.org/10.29252/jafm.11.06.28831

Belblidia, F., Keshtiban, I. J., & Webster, M. F. (2003). Novel schemes for steady weakly compressible and incompressible flow s. *ACME-UK Conference*, University of Strathclyde, Glasgow, UK .

Bharti, Ram Prakash, Ram Pravesh Ram, Amit Kumar Dhiman. (2022). Computational analysis of cross-flow of power-law fluids through a periodic square array of circular cylinders. *Asia-Pacific Journal Chemical Engineering,* 17.2 e2748. https://doi.org/10.1002/apj.2748

Blanco, M., Battiato, J., & Disotell, K. J. (2019). *Sensitivity study of contraction flow for boundary-layer validation wind tunnel*. AIAA Aviation 2019 Forum (p. 3095). https://doi.org/10.2514/6.2019-3095

Boyd, J., Buick, J. M., Green, S. (2007). Analysis of the casson and carreau-yasuda non-newtonian blood models in steady and oscillatory flows using the lattice boltzmann method. *Journal of Physics in Fluids,* 19(9), 093103. https://doi.org/10.1063/1.2772250

Carer, C., Driever, L. X., Köbben, S., Mckenzie, M., Rhenman, F., Sype, O. V. D., & Jyoti, B. V.S. (2021). Effect of parameter variation on the viscosity of ethanol gel propellants. *Journal Aerosol Technology Managment*. 13. https://doi.org/10.1590/jatm.v13.1196

Crank, J., & Nicolson, P. (1996). A practical method for numerical evaluation of solutions of partial differential equations of the heat-conduction type. *Advances in Computational Mathematics*, 6(1), 207-226. https://doi.org/10.1007/BF02127704

Hawken, D. M., Tamaddon-Jahromi, H. R., Townsend, P., & Webster, M. F. (1990). Galerkin based algorithm for viscous incompressible flow. *International Jornal for Numerical Methods in Fluids*, 10 (1990), 327-351. https://doi.org/10.1002/fld.1650100307

Fadhel, I. A., & Al-Muslimawi, A. H. (2020). Simulation of Newtonian axisymmetric pipe flow by using a Taylor Galerkin/pressure correction finite element

method. *Basrah Journal of Science*, 38(2), 198-222. https://doi.org/10.29072/basjs.202024

Ferrás, L. L., Afonso, A. M., Alves, M. A., Nóbrega, J. M., Carneiro, O. S., & Pinho, F. T. (2014). Slip flows of Newtonian and viscoelastic fluids in a 4: 1 contraction. *Journal of Non-Newtonian Fluid Mechanics*, 214, 28-37 . https://doi.org/10.1016/j.jnnfm.2014.09.007

Galdi, G. (2011*). An introduction to the mathematical theory of the Navier-Stokes equations: Steady-state problems*. Springer Science & Business Media.

Graham, D. I., & Jones, T. E. R. (1994). Settling and transport of spherical particles in power-law fluids at finite Reynolds number. *Journal of Non-Newtonian Fluid Mechanics*, 54, 465-488. https://doi.org/10.1016/0377-0257(94)80037-5

Haward, S. J., Li, Z., Lighter, D., Thomas, B., Odell, J. A., & Yuan, X. F. (2010). Flow of dilute to semi-dilute polystyrene solutions through a benchmark 8: 1 planar abrupt micro-contraction. *Journal of Non-Newtonian Fluid Mechanics,* 165(23-24), 1654-1669. https://doi.org/10.1016/j.jnnfm.2010.09.002

Jeong, J., & Hussain, F. (1995). On the identification of a vortex. *Journal of Fluid Mechanics*, 285, 69-94.

Karimi, S., Dabagh, M., Vasava, P., Dadvar, M., Dabir, B., Jalali, P. (2014). Effect of rheological models on the hemodynamics within human aorta: CFD study on CT image-based geometry. *Journal of Non-Newtonian Fluid Mechanics,* 207, 42-52. https://doi.org/10.1016/j.jnnfm.2014.03.007

Karlson, M., Nita, B. G., & Vaidya, A. (2020). Numerical computations of vortex formation length in flow past an elliptical cylinder. *Fluids*, 5(3), 157. https://doi.org/10.3390/fluids5030157

Lanzaro, A., & Yuan, X. F. (2011). Effects of contraction ratio on non-linear dynamics of semi-dilute, highly polydisperse PAAm solutions in microfluidics. *Journal of Non-Newtonian Fluid Mechanics*, 166(17-18), 1064-1075. https://doi.org/10.1016/j.jnnfm.2011.06.004

Liepsch, D., Sindeev, S., & Frolov, S. (2018, August). *An impact of non-Newtonian blood viscosity on hemodynamics in a patient-specific model of a cerebral aneurysm.* Inernational Journal of Physics: Conference Series, IOP Publishing. https://doi.org/10.1088/1742-6596/1084/1/012001

López-Aguilar, J. E., Webster, M. F., Al-Muslimawi, A. H. A., Tamaddon-Jahromi, H. R., Williams, R., Hawkins, K., & Lewis, K. (2015). A computational extensional rheology study of two biofluid systems. *Rheologica Acta*, 54(4), 287-305. https://doi.org/10.1007/s00397-014-0830-y

Mahmood, R., Majeed, A. H., Tahir, M., Saddique, I., Hamadneh, N. N., Khan, I., Mehmood, A. (2022). Statistical analysis of hydrodynamic forces in power-law fluid flow in achannel: circular versus semi-circular cylinder. *Journal Frontiers in Physics*, 38. https://doi.org/10.3389/fphy.2022.830408

Patil, H., & Jeyakarthikeyan, P. V. (2018, August). *Mesh convergence study and estimation of discretization error of hub in clutch disc with integration of ANSYS.* IOP Conference Series: Materials Science and Engineering, IOP. Publishing. https://doi.org/10.1088/1757-899X/402/1/012065

Reddy, J. N. (2019). *Introduction to the finite element method*. McGraw-Hill Education.

Şahin, B., Ward-Smith, A. J., & Lane, D. (1995). The pressure drop and flow characteristics of wide-angle screened diffusers of large area ratio. *Journal of Wind Engineering and Industrial Aerodynamics*, 58(1-2), 33-50. https://doi.org/10.1016/0167-6105(95)00018-M

Schäfle, C., & Kautz, C. (2019). *Students reasoning in fluid dynamics: Bernoulli's principle vs. the continuity equation.* Proceedings of the 10th International Conference on Physics Teaching in Engineering Education

Sharhanl, A. A., & Al-Muslimawi, A. (2021). Numerical simulation of a power-law inelastic fluid in axisymmetric contraction by using a Taylor Galerkin-pressure correction finite element method. *International Journal of Nonlinear Analysis and Applications*, 12, 2211- 2222. https://doi.org/10.22075/IJNAA.2021.6113.

Sousa, P. C., Coelho, P. M., Oliveira, M. S. N., & Alves, M. A. (2011). Effect of the contraction ratio upon viscoelastic fluid flow in three-dimensional square–square contractions. *Chemical Engineering Science*, 66(5), 998-1009. https://doi.org/10.1016/j.ces.2010.12.011

Tanner, R. I. (2000). *Engineering rheology*.OUP Oxford.

Thohura, S., Molla, M. M., & Sarker, M. M. A. (2019). Numerical simulation of non-Newtonian power-law fluid flow in a lid-driven skewed cavity. *International Journal of Applied and Computational Mathematics*, 5, 1-29. https://doi.org/10.1007/s40819-018-0590-y

Thorne, K. S., & Blandford, R. D. (2017). *Modern classical physics: optics, fluids, plasmas, elasticity, relativity, and statistical physics*. Princeton University Press. https://doi.org/10.1080/00107514.2018.1515249

Walker, J., Halliday, D., & Resnick, R. (2011). *Principles of Physics*. Hoboken, NJ: Wiley.

Yasir, R. Y., Al-Muslimawi, A. H., Jassim, B. K. (2020). Numerical simulation of non-Newtonian inelastic flows in channel based on artificial compressibility method. *Journal of Applied Computational Mechancs*, 6(2), 271-283. https://doi.org/10.22055/JACM.2019.29948.1650